The Astrophysical Journal Letters, 988:L50 (6pp), 2025 August 1 https://doi.org/10.3847/2041-8213/adeca8

Contemporaneous X-Ray and Optical Polarization of Extremely High-synchrotron-peaked Blazar H 1426+428

Anuvab Banerjee[1], Akash Garg[2], Divya Rawat[3], Svetlana Jorstad[4,5], Alan P. Marscher[4], Ivan Agudo[6], Jorge Otero-Santos[6,7], Daniel Morcuende[6], Juan Escudero Pedrosa[6,8], Alberto Domínguez[9], Ayan Bhattacharjee[10], Isaiah Cox[1], Indrani Pal[1], Xiurui Zhao[11,12], Andrealuna Pizzetti[13], Stefano Marchesi[1,14,15], Núria Torres-Albà[16], Kouser Imam[1], Ross Silver[17], and Marco Ajello[1]
[1] Clemson University, Clemson, SC 29634, USA
[2] Inter-University Center for Astronomy and Astrophysics, Ganeshkhind, Pune 411007, India
[3] Observatoire Astronomique de Strasbourg, Université de Strasbourg, CNRS, 11 rue de l'Universite, F-67000 Strasbourg, France
[4] Institute for Astrophysical Research, Boston University, 725 Commonwealth Avenue, Boston, MA 02215, USA
[5] Saint Petersburg State University, 7/9 Universitetskaya nab., 199034 St. Petersburg, Russia
[6] Instituto de Astrofísica de Andalucía (CSIC), Glorieta de la Astronomía s/n, 18008 Granada, Spain
[7] Istituto Nazionale di Fisica Nucleare, Sezione di Padova, 35131 Padova, Italy
[8] Center for Astrophysics, Harvard & Smithsonian, Cambridge, MA 02138, USA
[9] IPARCOS and Department of EMFTEL, Universidad Complutense de Madrid, E-28040 Madrid, Spain
[10] Research Institute of Basic Sciences, Seoul National University, Seoul 08826, Republic of Korea
[11] Department of Astronomy, University of Illinois at Urbana-Champaign, Urbana, IL 61801, USA
[12] Cahill Center for Astrophysics, California Institute of Technology, 1216 East California Boulevard, Pasadena, CA 91125, USA
[13] European Southern Observatory, Alonso de Córdova 3107, Casilla 19, Santiago 19001, Chile
[14] Dipartimento di Fisica e Astronomia (DIFA), Università di Bologna, via Gobetti 93/2, I-40129 Bologna, Italy
[15] INAF, Osservatorio di Astrofisica e Scienza dello Spazio di Bologna, via P. Gobetti 93/3, 40129 Bologna, Italy
[16] Department of Astronomy, University of Virginia, P.O. Box 400325, Charlottesville, VA 22904, USA
[17] NASA Goddard Space Flight Center, Greenbelt, MD 20771, USA
Received 2025 January 27; revised 2025 July 3; accepted 2025 July 6; published 2025 July 23

Abstract

We present the first contemporaneous X-ray and optical polarimetric measurement of the extremely high-synchrotron-peaked (HSP) blazar H 1426+428. The X-ray polarimetric observations were undertaken using the Imaging X-ray Polarimetry Explorer (IXPE) on 2024 May 27 and 2024 July 5. The IXPE pointings were accompanied by contemporaneous optical observations of the Observatorio de Sierra Nevada, Calar Alto Observatory, and the Perkins Telescope Observatory. While we observed the X-ray degree of polarization to be >20%, the polarization in the optical band was found to be only 1%–3%. This trend has been observed in several HSP blazars with available optical and X-ray polarimetric data and is typically explained in terms of energy stratification downstream of a shock. However, we observed a significant difference between the optical and X-ray polarization angles, a feature that has been observed in certain HSP blazars, such as Mrk 421, but remains a relatively rare or underreported phenomenon. We discuss possible scenarios for these findings within the framework of a partially turbulent jet model.

Unified Astronomy Thesaurus concepts: Blazars (164)

1. Introduction

Blazars are a subclass of active galactic nuclei whose powerful jets are oriented toward our line of sight (e.g., C. M. Urry & P. Padovani 1995). The electromagnetic emission from such objects spans the entire electromagnetic spectrum, ranging from lower-energy radio to very high-energy γ-rays (T. Hovatta & E. Lindfors 2019). The broadband spectral energy distribution of blazars is characterized by a double-hump shape, with the low-energy synchrotron emission peak in the infrared/X-ray regime and the higher energy peak in the MeV–GeV regime (G. Fossati et al. 1998). High-synchrotron-peaked (HSP) blazars form a subclass with synchrotron peaks occurring at frequencies $\geqslant 10^{15}$ Hz, i.e., in the UV/X-ray regime (A. Abdo et al. 2010). An HSP blazar with synchrotron peak frequency occurring at frequencies $\nu_{\rm syn} \sim 10^{17}$ Hz is termed an extreme HSP (EHSP) blazar (P. Giommi et al. 1999; V. S. Paliya et al. 2019; M. Nievas Rosillo et al. 2022).

With the launch of the Imaging X-ray Polarimetry Explorer (IXPE; M. C. Weisskopf et al. 2022), comprehensive broadband polarization measurements of blazars from radio to X-rays have become possible, which has enabled the community to infer the particle acceleration properties in blazar jets (L. Di Gesu et al. 2022, 2023; I. Liodakis et al. 2022). Since the X-ray emission is associated with the high-energy electrons close to the acceleration site, such measurements are extremely crucial (C.-T. J. Chen et al. 2024). The first of such measurements on the well-known blazar source Mrk 501 revealed the degree of polarization (PD hereafter) in X-ray to be ∼10%, higher compared to the optical polarization (∼4%–5%), with the polarization angle (PA hereafter) oriented parallel to the jet axis (I. Liodakis et al. 2022). The result can be interpreted in terms of the synchrotron emission arising out of the diffusive shock acceleration of an energy-stratified electron population. As the high-energy electrons propagate away from the acceleration site, they sample more turbulent segments of the jet, and consequently, the optical and

Table 1
Full Observation Log for H 1426+428

Instrument	ObsID	Tstart (MJD)	Tstop (MJD)	Exposure (ks)
IXPE	03007201	60457.33	60459.50	105.8
IXPE	03007301	60496.66	60498.83	104.4
Swift-XRT	00035020021	60457.05	60457.66	1.6
Swift-XRT	00030375219	60496.18	60496.25	1.9

Note. The columns represent the instruments used, the corresponding observation IDs, the start and end time for observation (in MJD), and the exposure times.

radio emission becomes less polarized. Such a trend is observed in several other HSP blazars, including Mrk 421 (L. Di Gesu et al. 2022). However, in general, there does not seem to be an obvious relationship between the PA and the radio jet position angle. A mismatch between the PA and the jet orientation has been detected in some blazar sources (e.g., 1ES 0229+200; S. R. Ehlert et al. 2023), while evidence of time variability of the PA has been observed in Mrk 421 (L. Di Gesu et al. 2023).

H 1426+428 is categorized as an EHSP source with its synchrotron peak lying in the X-ray region ($\nu_{\rm syn} \sim 10^{18}$ Hz; Y.-L. Chang et al. 2019). The source is bright enough in the optical (R mag = 14.4; M.-P. Véron-Cetty & P. Véron 2010) to allow for optical polarimetric observations from ground-based optical facilities. The source is also bright in X-ray with a flux $\geqslant 2.3 \times 10^{-11}$ erg cm^{-2} s^{-1} in the 2–8 keV band, which allows polarimetric measurements using IXPE. In addition, H 1426+428 is a TeV-detected HSP blazar (F. Aharonian et al. 2002; J. Quinn & VERITAS Collaboration 2021). At a redshift of $z = 0.129$ (R. Remillard et al. 1989), H 1426+428 is relatively close, allowing for detailed studies of its broadband emission without excessive extragalactic background light attenuation (e.g., A. Saldana-Lopez et al. 2021; A. Domínguez et al. 2024). Its proximity helps in studying environments of nearby galaxies with active blazars, which could help contextualize the evolution of similar sources at higher redshifts. For this source, particle acceleration by shock and magnetic reconnection has been proposed as an operative mechanism based on the intraday variability signatures in X-ray (P. Devanand et al. 2022) and optical (X. Chang et al. 2024) domains. Therefore, a comparison between optical and X-ray polarimetric signatures can break the degeneracy regarding the operative acceleration mechanism for this source.

In this Letter, we report the results of the first IXPE monitoring observation of H 1426+428. In Section 2, we provide the details of the observation. In Section 3, we present the results, and in Section 4, we draw our conclusions.

2. Observations and Data Analysis

For the purpose of our analysis, we have used contemporaneous Swift X-Ray Telescope (XRT) and IXPE data. The analysis has been undertaken using the FTOOLS software package HeaSoft version HEADAS-6.32 and XSPEC (K. A. Arnaud 1996) version 12.13.1, with the latest calibration database (CALDB). The details of the observation for each instrument are provided in Table 1. Below, we describe the reduction and analysis techniques used in this work.

2.1. IXPE

IXPE[18] has observed H 1426+428 on 2024 May 27 and 2024 July 5, for a total exposure of ∼210 ks (proposal no: 1186, PI: A. Banerjee). For the scientific analysis, we use cleaned and calibrated LEVEL-2 event files for all the detector units (DUs) obtained from the High Energy Astrophysics Science Archive Research Center archive. In order to choose the appropriate source and background regions, we extract the imaging data from the event files using the FTOOLS task XSELECT and plot using the plotting software DS9. The IXPE LEVEL-2 photon event list has been processed through the rejection algorithm of A. Di Marco et al. (2023)[19] in order to reduce the instrumental background. We consider a circular region of 60″ radius centered on the source position to be the "source" region and another concentric annular region between 150″ and 300″ to be the background region. These regions are employed in the XPSELECT tool of IXPEOBSSIM 31.0.3[20] (L. Baldini et al. 2022) in order to produce cleaned source and background event files for all DUs. We use the latest response file IXPE:OBSSIM20240101:V13 for this purpose. In order to extract the polarization properties, different binning algorithms of XPBIN are employed. The model-independent PD and PA are estimated using the PCUBE algorithm (F. Kislat et al. 2015), while XSPEC readable count I and Stokes Q and U spectra are generated using the algorithms PHA1, PHA1Q, and PHA1U, respectively.

The I, Q, and U spectra are then rebinned using FTGROUPPHA, where I spectra are first binned using an optimal binning algorithm employing the response matrix and Stokes spectra are subsequently binned using the I spectrum as a template file.

2.2. Swift-XRT

Swift-XRT (D. N. Burrows et al. 2005) is an X-ray imaging telescope operating at 0.2–10 keV with an effective area of ∼125 cm^{-2} at 1.5 keV. Contemporaneously with IXPE, Swift-XRT observed the source for ∼3.5 ks. The XRTPIPELINE task is employed to extract the clean event files, and source and background spectra are generated using XSELECT. In order to extract the source spectra, we consider a circle of 15″ radius centered on the source position, and for background, we consider a circular region of radius 40″ away from the source position. The spectra are rebinned to ensure a minimum of 5 counts in each bin using the FTOOLS task GRPPHA. In order to build the Ancillary Response Files, we have used the task XRTMKARF for every spectral file.

3. Results

We have undertaken both model-independent (PCUBE) and spectropolarimetric (using XSPEC) procedures to explore the polarization features of H 1426+428. In the former model-independent approach, the I, Q, and U parameters are computed via summing over the observed photoelectric

[18] IXPE is capable of measuring the polarization properties, as well as spectral and temporal properties, of X-ray sources in the 2–8 keV band (M. C. Weisskopf et al. 2022).
[19] https://github.com/aledimarco/IXPE-background.git
[20] https://ixpeobssim.readthedocs.io/en/latest/

Table 2
The PD and PA for H 1426+428 Using All DUs, Along with 1σ Error for 1 Degree of Freedom, Extracted Using the PCUBE Algorithm

Obs.		2–8 (keV)	2–4 (keV)	4–6 (keV)	6–8 (keV)
03007201	PD (%)	8.7 ± 5.2	3.7 ± 4.1	13.8 ± 9.8	78.9 ± 3.0
(2024 May 27)	PA (deg)	21.9 ± 16.9	52.4 ± 32.7	22.7 ± 20.3	7.9 ± 11.7
	MDP_{99} (%)	15.6	14.1	29.7	94.5
03007301	PD (%)	20.3 ± 4.1	18.0 ± 3.7	18.3 ± 7.2	46.1 ± 19.5
(2024 Jul 5)	PA (deg)	−60.6 ± 5.7	−61.6 ± 5.9	−65.5 ± 11.3	−53.1 ± 12.3
	MDP_{99} (%)	12.2	11.1	21.9	59.9

emission angle for each IXPE event, and PD and PA values are subsequently recovered. In XSPEC, on the other hand, radiative models and polarization models (such as POLCONST) are employed together to fit the count and Stokes spectra, and from the spectral fit PD and PA values are obtained.

3.1. PCUBE Analysis

Our results show that the source is in a relatively higher flux state ($F_{0.3-10\ \mathrm{keV}} = (5.2 \pm 0.2) \times 10^{-11}$ erg cm^{-2} s^{-1}) on 2024 July 5 (O2 hereafter) compared to 2024 May 27 (O1 hereafter), where the flux level was $F_{0.3-10\ \mathrm{keV}} = (4.1 \pm 0.3) \times 10^{-11}$ erg cm^{-2} s^{-1}. As shown in Table 2, the detectable polarization level is different in these two flux states. In the case of O1, in the 2–8 keV band, the PD values are calculated to be 8.7% ± 5.2%, which are below the threshold given by $MDP_{99} = 15.6\%$. We therefore consider the PD in O1 to be undetected. On the other hand, in the case of O2, the PD in 2–8 keV is found to be 20.3% ± 4.1%, and with $MDP_{99} = 12.2\%$, we conclude that in the second observation, polarization is significantly measured. There is an indication of a PA shift from O1 ($\sim 22^\circ$) to O2 ($\sim -61^\circ$). However, since PD in O1 is undetected, the PA value in O1 cannot be treated as significant. The measurements from all the detectors have been summed up to enhance the confidence interval over PD and PA. In Figure 1, we show the 1σ, 2σ, and 3σ confidence contour plots as well as MDP_{99} for O1 and O2 in the PD–PA plane in 2–8 keV, and corresponding values are listed in Table 2. Unless explicitly mentioned, the reported error corresponding to each parameter indicates 1σ confidence level. We have also checked the lightcurves for the presence of variability, but they do not show any significant evidence of intraobservation variability.

To investigate the dependence of PA and PD with energy, we measure the PD and PA values in three energy bands (2–4, 4–6, and 6–8 keV) using the PCUBE algorithm. As shown in Table 2, except for the 2–4 keV in O2, the PD values in all the sub-bands lie consistently below MDP_{99}, therefore preventing us from concluding any energy dependence of PD.

3.2. XSPEC Analysis

In order to explore the basic radiative properties of H 1426 +428 during the two observations, we start the spectral fitting of the joint Swift-XRT and IXPE spectra in the using the model combination TBABS*(POWERLAW), where TBABS is the multiplicative model representing the interstellar absorption, and the POWERLAW component represents the multicolor nonthermal Compton emission from the source. For the purpose of our analysis, we fix the interstellar absorption at 9.59×10^{19} cm^{-2} (obtained via the HeaSoft hydrogen column density calculator[21]). The fitting yields a χ^2 of 563.4 for 309 dof and 658.6 for 311 dof, corresponding to O1 and O2, respectively.

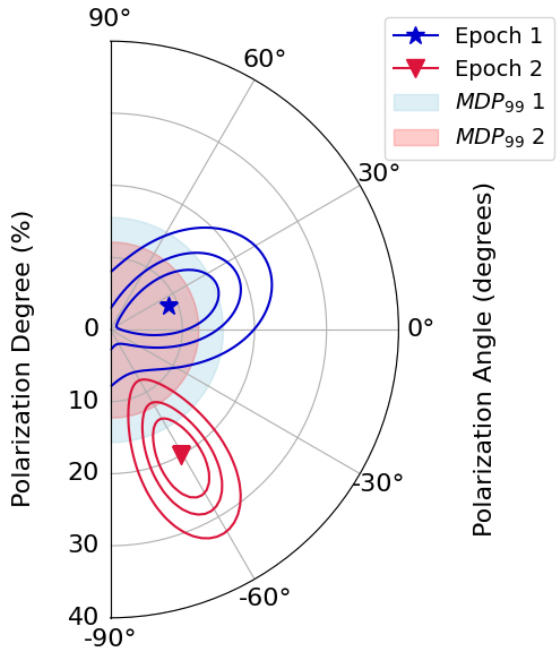

Figure 1. Contour plots of PD and PA for H 1426+428 in the 2–8 keV band using PCUBE algorithm after summing up events from all DUs. The three contours (from inner to outer) represent 1σ, 2σ, and 3σ confidence levels. The blue and pink solid semicircles indicate MDP_{99} for the first and second observations, respectively. It is apparent that the degree of polarization as obtained from PCUBE is lower compared to MDP_{99} during the first measurement but is higher than MDP_{99} during the second measurement.

Subsequently, we fit the *I* spectra from Swift-XRT and *Q*, *U* spectra from IXPE simultaneously. We attempt the model combination TBABS*CONST*POLCONST*(POWERLAW), where POLCONST is a multiplicative, energy-independent model for polarization, and CONST takes care of the cross-calibration factor between Swift-XRT and IXPE spectra. The fit yielded a χ^2 of 278.4 for 309 dof and 294.2 for 311 dof, corresponding to O1 and O2, respectively. In the case of O1, PD and PA are found to be 2.4% ± 1.5% and $39.^\circ5 \pm 33.^\circ4$, respectively. However, since we could not detect PD using the PCUBE algorithm, the comparison between PCUBE and XSPEC results could not be made in the case of O1. In O2, the PD value is calculated to be 7.0% ± 2.1%, and PA is calculated to be $-62.^\circ4 \pm 7.^\circ5$. We see the PD value does not overlap with the corresponding PCUBE result within the uncertainty.

[21] https://heasarc.gsfc.nasa.gov/cgi-bin/Tools/w3nh/w3nh.pl

Table 3
Best Fit Spectral Parameters for Swift-XRT and IXPE Data Using TBABS*CONST*POLCONST*POWERLAW as well as TBABS*CONST*POLPOW*POWERLAW Combination

Component	Parameter	Value (2024 May 27)	Value (2024 Jul 5)
power law	Γ	1.85 ± 0.44	1.7 ± 0.4
power law	norm (10^{-3})	17.1 ± 1.9	5.0 ± 1.0
polconst	PD (%)	2.4 ± 1.5	7.0 ± 2.1
polconst	PA (deg)	39.5 ± 33.4	-62.4 ± 7.6
χ^2/dof		278.4/309	294.2/311
polpow	PD (%)	7.6 ± 6.2	13.6 ± 2.9
polpow	PA (deg)	30.7 ± 26.1	-62.5 ± 7.5
χ^2/dof		278.5/309	292.6/311

Note. The errors for the power-law model correspond to 99% confidence on the model parameters. For polpow and polconst models, we report 1σ error for 1 degree of freedom.

In order to resolve the discrepancy between PCUBE and XSPEC results, we further test our spectral fitting using the energy dependent polarization (POLPOW) model. According to the POLPOW model, $\mathrm{PD}(E) = \mathrm{PD}_{\mathrm{norm}} \times E^{-\alpha_{\mathrm{PD}}}$, and $\mathrm{PA}(E) = \psi_{\mathrm{norm}} \times E^{-\alpha_{\mathrm{PA}}}$, where $\mathrm{PD}_{\mathrm{norm}}$ is the PD at 1 keV with α_{PD} being the corresponding index. Similarly, ψ_{norm} is the PA at 1 keV with α_{PA} being the corresponding index. Since we do not observe energy dependence of PA, we pivot the index of PA to zero. This yields the best-fit spectra with $\chi^2/\mathrm{dof} = 278.5/309$, $A_{\mathrm{PD}} = 0.02 \pm 0.01$, $\alpha_{\mathrm{PD}} = -0.14 \pm 0.07$ for O1, and $\chi^2/\mathrm{dof} = 292.6/311$, $A_{\mathrm{PD}} = 0.04 \pm 0.01$, $\alpha_{\mathrm{PD}} = -0.39 \pm 0.8$ for O2. As previously mentioned, comparison between PCUBE and XSPEC results could not be undertaken for O1 due to the nondetection of polarization. For O2, the model is integrated in 2–8 keV with the best-fit parameters to obtain the PD $\sim$ 13% and PA $\sim -62^\circ$. This matches with the PCUBE result within the uncertainty limit.

In Table 3, we provide the best-fit parameters alongside the respective errors obtained using *XSPEC* fitting. The simultaneously fitted *I*, *Q*, and *U* spectra for all the DUs as well as the residuals pertaining to the observation on 2024 May 27 are shown in Figure 2.

3.3. Results from Optical Polarimetry

During the IXPE pointings, we coordinated an optical campaign with Observatorio de Sierra Nevada (OSN), Calar Alto Observatory (CAHA), and the 1.8 m Perkins Telescope to obtain contemporaneous polarimetric data in the optical domain. Photometric observations from OSN were obtained in the *R* band using the DIPOL-1 instrument installed at the 0.9 m T90 telescope and analyzed using standard procedures (J. Otero-Santos et al. 2024). The photometric *BVRI* data from OSN were taken with the 1.5 m T150 telescope. We also obtain data from CAHA captured with the CAFOS instrument installed on the 2.2 m telescope, which allows for photopolarimetric observations. The polarimetry was performed in the *R* band, with additional photometric *BVRI* observations (J. Escudero Pedrosa et al. 2024). *R*-band polarimetric observations as well as *BVRI* photometry were carried out using the PRISM camera mounted on the Perkins Telescope Observatory employing the polarimetric analysis procedures as described in S. G. Jorstad et al. (2010) and differential photometry with the comparison stars 1, 2, and 3 from P. S. Smith et al. (1991) to estimate polarization parameters and brightness. During both O1 and O2, the *R*-band magnitude lies within $\sim$15–16, which agrees with the previously observed magnitude for the target (R. Remillard et al. 1989). During both O1 and O2, the *R*-band polarization degree is found to be much lower (<3%) compared to the X-ray polarization degree. Also, the PA in optical during O2 differs significantly from the PA in X-ray. The details of optical magnitude, polarization degree, and angle during the observation campaign are provided in Table 4.

4. Discussion and Summary

We have presented the first IXPE observations of the TeV-detected EHSP blazar H 1426+428 obtained in 2024. All of our observations were complemented with contemporaneous optical and Swift/XRT campaigns. During the $\sim$40 day difference between the two observations, the source demonstrated an enhancement in X-ray flux. During our first observation on 2024 May 27, the polarization degree and angle remained undetected. However, during the second IXPE pointing on 2024 July 5, significant (>20%) polarization in X-ray could be detected with >99% confidence. The X-ray PD values were found to be significantly higher compared to those in the optical.

The higher X-ray PD measurements compared to those in other wavelengths are common among IXPE-observed HSP blazars, and have been observed in several cases, e.g., Mrk 421 (L. Di Gesu et al. 2022; A. M. Bharathan et al. 2024), Mrk 501 (C.-T. J. Chen et al. 2024), 1ES 0229+20 (S. R. Ehlert et al. 2023), and 1ES 1959+65 (M. Errando et al. 2024). The increasing PD from optical to X-ray is generally interpreted in terms of acceleration of high-energy electrons across shock. Higher-energy photons emitted in X-ray are generated by synchrotron emission from electrons in the immediate downstream of the shock front, while lower-energy photons such as optical are generated by electrons further downstream because of the longer radiative cooling time, where they are subjected to the more turbulent component of the magnetic field (A. P. Marscher & W. K. Gear 1985; A. P. Marscher & S. G. Jorstad 2021). Within the X-ray domain, we attempt to decipher any plausible dependence of PD on energy. During both of our observations, the energy-resolved PD values lie below MDP_{99}, and consequently, we cannot make any definitive claim of energy dependence. In the optical domain, since we measure the polarization value only in the *R* band, we are unable to infer any energy dependence of polarization. We also note that the detected polarization ($\sim$20%) in X-ray is far lower than the synchrotron limit. With a power-law energy spectrum of relativistic electron of the form $N(E) \propto E^{-p}$ with p being the spectral index, the expected PD is $\sim \frac{p+1}{p+7/3} \sim 70\%$ for $p = 2$ and $\sim$75% for $p = 3$, if the relativistic electrons are in a site of homogeneous magnetic field (G. B. Rybicki & A. P. Lightman 1991). Within a region of the jet where the fraction of the ordered component of the magnetic field is f_{ord}, the mean PD is given by

$$\langle P \rangle \propto [f_{\mathrm{ord}}^2 + (1 - f_{\mathrm{ord}})^2 N^{-1}(\nu)]^{1/2}, \quad (1)$$

where the number of turbulent cells involved in the emission at frequency ν is $N(\nu) \sim \nu^{-1/2}$ (A. P. Marscher & S. G. Jorstad 2022). In case the disordered component of the magnetic field

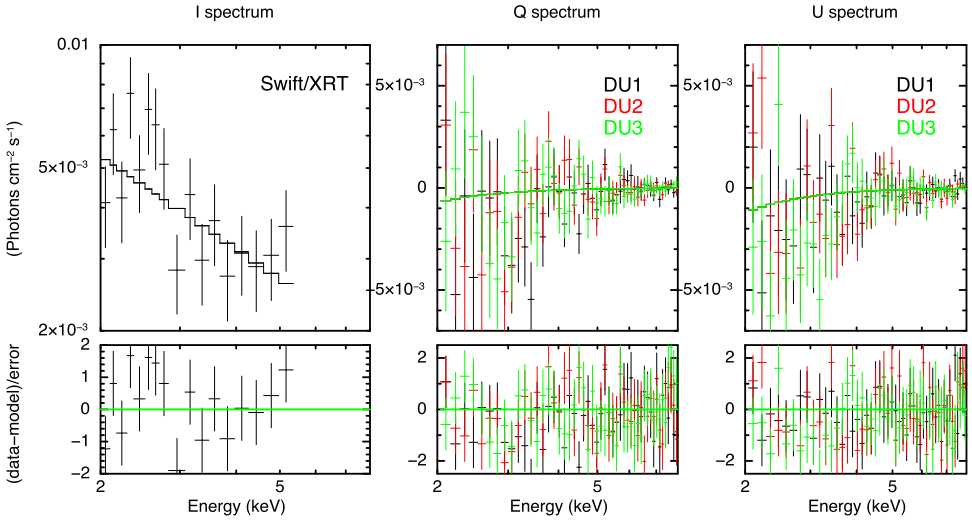

Figure 2. Top-left panel shows the XSPEC fit of Swift-XRT spectra using a power-law model corresponding to the observation on 2024 May 27. The top-middle and top-right panels show the simultaneous fit of Stokes Q and U spectra, respectively, including all DUs. Bottom panels show the corresponding fit residuals.

Table 4
Details of Optical Polarimetric Measurements

Obs. Date	Magnitude	PD (%)	PA (deg)
2024 May 27	15.91 ± 0.04	1.56 ± 0.27	38.6 ± 4.6
2024 May 28	15.90 ± 0.01	1.49 ± 0.13	48.3 ± 5.4
2024 Jul 5	15.95 ± 0.02	2.47 ± 0.06	74.1 ± 5.0
2024 Jul 6	15.95 ± 0.02	1.87 ± 0.07	75.6 ± 4.4

Note. Pertaining to each observation, we provide the magnitude, degree, and angle of polarization.

dominates the ordered component, we can expect $P \sim \nu^{1/4}$. Therefore, we would expect a higher PD in the X-ray domain compared to optical. In the X-ray band, we have $\nu \sim 10^{18}$, while in the optical R band, $\nu \sim 4.6 \times 10^{14}$. If we consider the ratio, then $P_X/P_O \sim (\text{ratio})^{1/4} \sim 6.8$. Given we are getting $\sim$2% polarization in the optical, $P_X \sim 13.6\%$ matches up with the P_X value as determined from the spectral fit (within uncertainties). This implies that the X-ray emission originates from a partially ordered (by shock compression) region close to the shock acceleration site, while the optical emission arises from a more strongly turbulent region farther from the shock, which reduces the PD (A. P. Marscher & S. G. Jorstad 2021, 2022). Recent high-resolution 3D radiative hydrodynamic simulations of relativistic jets also show such shock mediated onset of turbulence, and a corresponding rise in the turbulent component of the estimated magnetic field (A. Bhattacharjee et al. 2024).

In our analysis, we observe a change in the PA in the optical domain, while in the X-ray domain, we measure the PA only during O2. Substantial rotation of PA in X-ray has previously been detected only in the case of Mrk 421 so far (L. Di Gesu et al. 2023), although a number of optical rotations have been reported in the literature (D. Blinov et al. 2016). One specific model to explain such a feature is the propagation of a magnetosonic shock along the direction of a helical magnetic field in the jet, where the rate of PA rotation is determined by the time taken by the shock to cross one full pitch (H. Zhang et al. 2016). Another interesting scenario supporting PA rotation could be the compression of the magnetic field structure in the postshock region, where the ordered component of the field dominates the turbulent component (E. Angelakis et al. 2016). However, in order to confirm such a scenario, simultaneous Very Long Baseline Array (VLBA) observation of the PA in the radio domain is necessary. In a previous VLBA campaign on TeV blazars during the years 2001–2004, a faint jet extending to the northwest, with a position angle of about -25°, was obtained for our source of interest at 8.4 GHz (B. G. Piner et al. 2008), which is roughly orthogonal to the PA in the optical domain as per our observation. In previous IXPE observations of HSP blazars, the PA in the optical roughly aligns with the jet position angle (I. Liodakis et al. 2022; S. Abe et al. 2024), although large rotations in the PA have also been observed (L. Di Gesu et al. 2023; R. Middei et al. 2023). Alignment of the optical PA with the jet position angle in the case of BL Lac objects is generally interpreted in the shock-compressed scenario where the ordered magnetic field is aligned perpendicular to the jet axis (A. P. Marscher & S. G. Jorstad 2021). Misalignment between the jet direction and PA is generally attributed to plausible local disturbances (B. G. Piner & P. G. Edwards 2005). Although we now have growing evidence that the position angle of radio jets can change over time, e.g., OJ 287 (S. Britzen et al. 2018), PG 1553+113 (R. Lico et al. 2020), and so on (Z. R. Weaver et al. 2022), in the absence of the simultaneous VLBA data, we are unable to confirm if the position angle is along the projected jet direction, or if the PA is off-axis relative to the jet. Models of turbulent plasma undergoing a shock transition can explain the alignment of the PA with the jet axis (A. P. Marscher 2014; F. Tavecchio 2021). Further multiwavelength observation with simultaneous VLBA campaigns is therefore crucial to confirm or reject such a hypothesis.

The significantly higher polarization in the X-ray domain compared to the optical obtained in our study, therefore, strongly supports the energy-stratified shock acceleration scenario in the HSP blazar jets. Observation of the rotation of the PA indicates the plausibility of the propagation of shocked plasma along a section of the jet with a helical magnetic field.

Acknowledgments

We thank the anonymous referee for constructive suggestions that have improved the quality of the manuscript. A.B. and M.A. acknowledge funding under NASA contract 80NSSC24K1745. J.O.S. acknowledges financial support from the project ref. AST22_00001_9 with founding from the European Union—NextGenerationEU, the Ministerio de Ciencia, Innovación y Universidades, Plan de Recuperación, Transformación y Resiliencia, the Consejería de Universidad, Investigación e Innovación from the Junta de Andalucía, and the Consejo Superior de Investigaciones Científicas, as well as from INFN Cap. U.1.01.01.01.009. A.D. is thankful for the support of the Proyecto PID2021- 433126536OA-I00 funded by MCIN/AEI/10.13039/501100011033. The IAA-CSIC coauthors acknowledge financial support from MCIN/AEI/10.13039/501100011033 through the Center of Excellence Severo Ochoa award for the Instituto de Astrofíisica de Andalucía-CSIC (CEX2021-001131-S), and through grants PID2019-107847RB-C44 and PID2022-139117NB-C44. Some of the data are based on observations collected at the Observatorio de Sierra Nevada, which is owned and operated by the Instituto de Astrofìsica de Andalucìa (IAA-CSIC). S. M.'s research activity is carried out with the contribution of the Next Generation EU funds within the National Recovery and Resilience Plan (PNRR), Mission 4—Education and Research, Component 2—From Research to Business (M4C2), Investment Line 3.1—Strengthening and creation of Research Infrastructures, Project IR0000012—"CTA+—Cherenkov Telescope Array Plus." Based on observations collected at Centro Astronómico Hispano en Andalucía (CAHA) at Calar Alto, proposals 24A-2.2-011 and 24B-2.2-015, operated jointly by Junta de Andalucìa and Consejo Superior de Investigaciones Cientìficas (IAA-CSIC). The research at Boston University was supported in part by the National Science Foundation grant AST-2108622. This study was based in part on observations conducted using the 1.8 m Perkins Telescope Observatory (PTO) in Arizona, which is owned and operated by Boston University. The scientific results reported in this Letter are based on observations made by the X-ray observatories Swift-XRT and IXPE. We acknowledge the use of the software packages DS9 and HEASoft.

ORCID iDs

Anuvab Banerjee https://orcid.org/0000-0001-7796-8907
Divya Rawat https://orcid.org/0000-0002-9280-2785
Svetlana Jorstad https://orcid.org/0000-0001-6158-1708
Alan P. Marscher https://orcid.org/0000-0001-7396-3332
Ivan Agudo https://orcid.org/0000-0002-3777-6182
Daniel Morcuende https://orcid.org/0000-0001-9400-0922
Alberto Domínguez https://orcid.org/0000-0002-3433-4610
Ayan Bhattacharjee https://orcid.org/0000-0002-2878-4025
Isaiah Cox https://orcid.org/0000-0003-2287-0325
Indrani Pal https://orcid.org/0000-0002-7825-1526
Xiurui Zhao https://orcid.org/0000-0002-7791-3671
Andrealuna Pizzetti https://orcid.org/0000-0001-6412-2312
Stefano Marchesi https://orcid.org/0000-0001-5544-0749
Núria Torres-Albà https://orcid.org/0000-0003-3638-8943
Kouser Imam https://orcid.org/0009-0003-3381-211X
Marco Ajello https://orcid.org/0000-0002-6584-1703

References

Abdo, A., Ackermann, M., Agudo, I., et al. 2010, ApJ, 716, 30
Abe, S., Abhir, J., Acciari, V., et al. 2024, A&A, 685, A117
Aharonian, F., Akhperjanian, A., Barrio, J., et al. 2002, A&A, 384, L23
Angelakis, E., Hovatta, T., Blinov, D., et al. 2016, MNRAS, 463, 3365
Arnaud, K. A. 1996, in ASP Conf. Ser. 101, Astronomical Data Analysis Software and Systems V, ed. G. H. Jacoby & J. Barnes (San Francisco, CA: ASP), 17
Baldini, L., Bucciantini, N., Di Lalla, N., et al. 2022, SoftX, 19, 101194
Bharathan, A. M., Stalin, C., Sahayanathan, S., et al. 2024, ApJ, 975, 185
Bhattacharjee, A., Seo, J., Ryu, D., & Kang, H. 2024, ApJ, 976, 91
Blinov, D., Pavlidou, V., Papadakis, I., et al. 2016, MNRAS, 457, 2252
Britzen, S., Fendt, C., Witzel, G., et al. 2018, MNRAS, 478, 3199
Burrows, D. N., Hill, J., Nousek, J., et al. 2005, SSRv, 120, 165
Chang, X., Xiong, D., Yi, T., et al. 2024, MNRAS, 533, 120
Chang, Y.-L., Arsioli, B., Giommi, P., Padovani, P., & Brandt, C. 2019, A&A, 632, A77
Chen, C.-T. J., Liodakis, I., Middei, R., et al. 2024, ApJ, 974, 50
Devanand, P., Gupta, A. C., Jithesh, V., & Wiita, P. J. 2022, ApJ, 939, 80
Di Gesu, L., Donnarumma, I., Tavecchio, F., et al. 2022, ApJL, 938, L7
Di Gesu, L., Marshall, H. L., Ehlert, S. R., et al. 2023, NatAs, 7, 1245
Di Marco, A., Soffitta, P., Costa, E., et al. 2023, AJ, 165, 143
Domínguez, A., Østergaard Kirkeberg, P., Wojtak, R., et al. 2024, MNRAS, 527, 4632
Ehlert, S. R., Liodakis, I., Middei, R., et al. 2023, ApJ, 959, 61
Errando, M., Liodakis, I., Marscher, A. P., et al. 2024, ApJ, 963, 5
Escudero Pedrosa, J., Agudo, I., Morcuende, D., et al. 2024, AJ, 168, 84
Fossati, G., Maraschi, L., Celotti, A., Comastri, A., & Ghisellini, G. 1998, MNRAS, 299, 433
Giommi, P., Menna, M., & Padovani, P. 1999, MNRAS, 310, 465
Hovatta, T., & Lindfors, E. 2019, NewAR, 87, 101541
Jorstad, S. G., Marscher, A. P., Larionov, V. M., et al. 2010, ApJ, 715, 362
Kislat, F., Clark, B., Beilicke, M., & Krawczynski, H. 2015, APh, 68, 45
Lico, R., Liu, J., Giroletti, M., et al. 2020, A&A, 634, A87
Liodakis, I., Marscher, A. P., Agudo, I., et al. 2022, Natur, 611, 677
Marscher, A. P. 2014, ApJ, 780, 87
Marscher, A. P., & Gear, W. K. 1985, ApJ, 298, 114
Marscher, A. P., & Jorstad, S. G. 2021, Galax, 9, 27
Marscher, A. P., & Jorstad, S. G. 2022, Univ, 8, 644
Middei, R., Perri, M., Puccetti, S., et al. 2023, ApJL, 953, L28
Nievas Rosillo, M., Domínguez, A., Chiaro, G., et al. 2022, MNRAS, 512, 137
Otero-Santos, J., Piirola, V., Pedrosa, J. E., et al. 2024, AJ, 167, 137
Paliya, V. S., Dominguez, A., Ajello, M., Franckowiak, A., & Hartmann, D. 2019, ApJL, 882, L3
Piner, B. G., & Edwards, P. G. 2005, ApJ, 622, 168
Piner, B. G., Pant, N., & Edwards, P. G. 2008, ApJ, 678, 64
Quinn, J. & VERITAS Collaboration 2021, ATel, 14501, 1
Remillard, R., Tuohy, I., Brissenden, R., et al. 1989, ApJ, 345, 140
Rybicki, G. B., & Lightman, A. P. 1991, Radiative Processes in Astrophysics (New York: Wiley)
Saldana-Lopez, A., Domínguez, A., Pérez-González, P. G., et al. 2021, MNRAS, 507, 5144
Smith, P. S., Jannuzi, B. T., Elston, R., et al. 1991, ApJS, 77, 67
Tavecchio, F. 2021, Galax, 9, 37
Urry, C. M., & Padovani, P. 1995, PASP, 107, 803
Véron-Cetty, M.-P., & Véron, P. 2010, A&A, 518, A10
Weaver, Z. R., Jorstad, S. G., Marscher, A. P., et al. 2022, ApJS, 260, 12
Weisskopf, M. C., Soffitta, P., Baldini, L., et al. 2022, JATIS, 8, 026002
Zhang, H., Deng, W., Li, H., & Böttcher, M. 2016, ApJ, 817, 63